SLEEP Advances, 2026, **7**, zpag012
doi:10.1093/sleepadvances/zpag012
Advance Access publication 28 January 2026
Original Article

Original Article

Rhythmic and arrhythmic components from local-field potentials during non-rapid eye movement sleep in younger and older mice

Jonathan Dubé [1,2,3], Justin Corbin[4], Jimmy Hernandez[2], Jean Marc Lina[2,4], Valérie Mongrain [5,6], Igor Timofeev [3,7] and Julie Carrier [1,2,*]

[1]Département de Psychologie, Université de Montréal, Montréal, Canada, [2]Hôpital du Sacré-Cœur de Montréal, Centre d'Études Avancées en Médecine du Sommeil, CIUSSS du Nord-de-l'Île-de-Montréal, Montréal, Canada, [3]Centre de Recherche CERVO, CIUSSS de la Capitale-Nationale, Quebec, Canada, [4]Département de Génie Électrique, École de Technologie Supérieure, Montréal, Canada, [5]Département de Neurosciences, Université de Montréal, Montréal, Canada, [6]Centre de Recherche du CHUM, Montréal, Canada and [7]Faculté de Médecine, Université Laval, Québec, Canada

*Corresponding author. Julie Carrier, Département de Psychologie, Université de Montréal, Montréal, Canada. Email: julie.carrier.1@umontreal.ca.

Abstract

The non-rapid-eye movement (NREM) sleep power spectrum is composed of rhythmic and arrhythmic components, respectively associated with brain rhythms and scale-free dynamics. Both components are hypothesized to represent distinct processes underlying sleep-dependent memory consolidation as well as other brain complex processes. Recent advancements in spectral parametrization techniques and the use of multifractal models have enabled new insights into these components and their connection to brain networks. Aging impacts NREM sleep oscillations, but no animal studies considered the impact of age on rhythmic and arrhythmic components. In this study, we assessed the effects of age on the power spectrum and its two components using local field potential recordings in mice. We recorded across the cerebral cortex and within the hippocampus—a central brain hub involved in NREM sleep-dependent cognitive processing. Ten younger (7.6 months) and eleven older (15.7 months) C57BL/6 J male and female mice were continuously recorded over a 24-hour period. We extracted the NREM sleep standard and rhythmic spectra, controlled for scale-free activity, and estimated multifractal arrhythmic properties during NREM sleep using the Wavelet Leader and Bootstrap based MultiFractal analysis toolbox. Older mice showed specific alterations in both components compared to younger animals: reduced rhythmic gamma power in the anterior cortex, greater regional differentiation of scaling exponents, and higher multifractal dispersion of the arrhythmic component in the hippocampus. These findings demonstrate that aging alters rhythmic and arrhythmic properties of NREM sleep in distinct brain regions, suggesting that both contribute to age-related changes in sleep-dependent cognition.

Key words: slow-wave sleep; electrophysiology; aging; animal models; EEG analysis; neuroscience; sleep and the brain; statistics

Submitted: 4 November, 2025; **Revised:** 6 January, 2026; **Accepted:** 7 January, 2026

Graphical Abstract

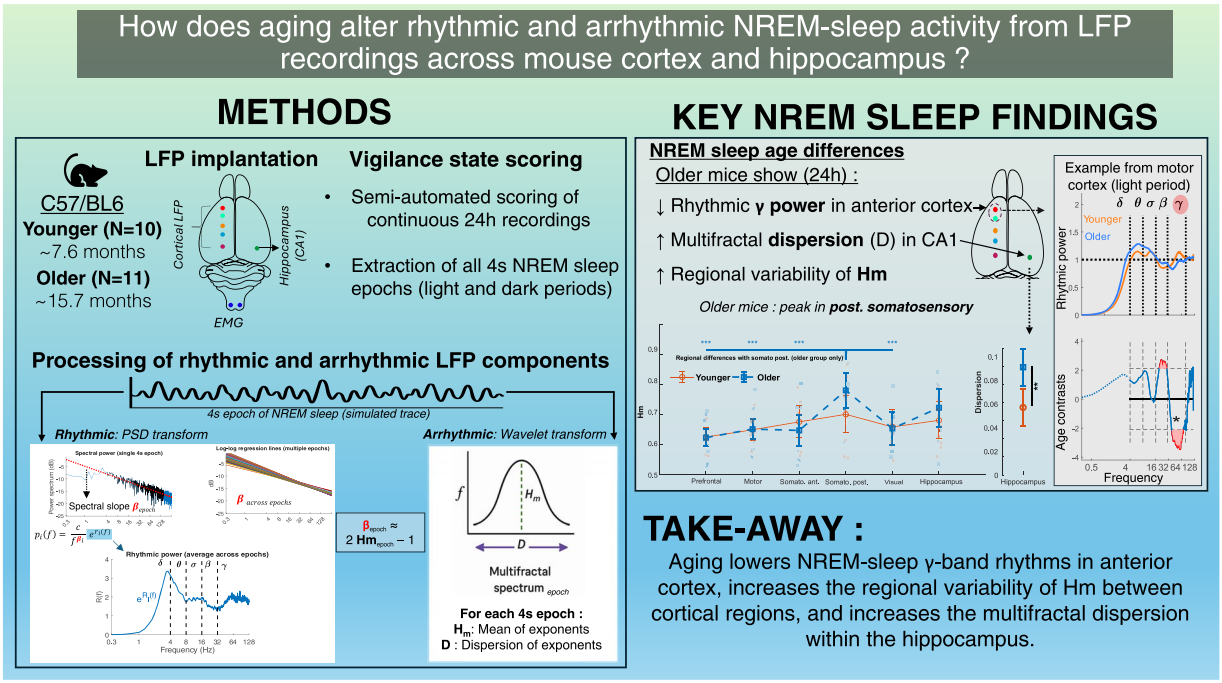

Statement of Significance

This study provides the first detailed examination of how normal aging affects rhythmic and arrhythmic components from the non-rapid eye movement (NREM) sleep power spectrum in mice, identifying specific changes in NREM sleep gamma rhythms from the anterior cortex, and in scale-free dynamics in the posterior cortex and in the hippocampus. These findings suggest that age-related changes in NREM sleep rhythms and scale-free dynamics expressed in specific regions may have distinct impacts on NREM sleep functions. Future research should further characterize both components during NREM sleep in the context of cognitive tasks to clarify their respective contribution to age-related changes in sleep-dependent cognitive function.

Introduction

Brain activity during non-rapid eye movement (NREM) sleep is characterized by thalamo-cortical and hippocampal oscillations, playing a pivotal role in neuronal plasticity and memory consolidation [1, 2]. Human studies showed that aging disrupts NREM sleep thalamocortical oscillations such as slow waves (delta; 0.5–4 Hz) and spindles (sigma; 12–16 Hz), and that oscillatory changes occurring particularly in frontal brain regions are associated with lower hippocampus-dependent memory consolidation [3–5]. Current theories suggest that age-related changes in frontal NREM sleep oscillations reflect altered frontal-hippocampal interactions during NREM sleep with aging [6]. As it is challenging to perform electrophysiological sleep recordings in the hippocampus of older humans, these theories have not been confirmed yet in humans. However, mouse models of aging are valuable for studying local neural dynamics in regions not easily accessible in humans, such as the hippocampus. Previous Alzheimer's disease mouse models reported age-related alterations in hippocampal activity during NREM sleep, but our understanding of the impact of aging on NREM sleep hippocampal activity is limited in mouse models of normal aging [7, 8].

Electroencephalogram (EEG) and electrocorticograph (ECoG) studies in non-pathological aging mouse models showed that C57BL/6 mice at 12 or 24 months of age exhibited higher slow-wave activity (SWA; 0.5–4 Hz) compared to younger mice [9, 10]. Local-field potential studies further highlighted that these differences are observed specifically in frontal brain areas [11, 12]. However, the effects of age on higher frequencies in posterior cortical regions and in the hippocampus during NREM sleep are not characterized in healthy mice.

Cerebral electrophysiological signals exhibit a rhythmic and an arrhythmic component in their power spectrum [13]. Narrowband peaks in the power spectrum represents a "rhythmic component" linked to recurrent brain oscillations, while its power-law shape indicates an arrhythmic scale-free component [14, 15]. Recent studies highlight the importance to account for the arrhythmic β slope when assessing narrowband rhythmic power [16, 17]. Formally, this is performed by modeling the power spectrum as resulting from two processes, which can be extracted and studied independently. Usually, the β slope of the power spectrum is estimated and attributed to the arrhythmic component, whereas the residual spectral power controlled for this slope is attributed to the rhythmic component. For instance, human studies using such model showed that age-related higher power in faster frequencies can be explained by a flatter (lower) arrhythmic β slope during wakefulness and during NREM sleep [13, 18–20]. Interestingly, higher SWA during NREM sleep in humans has been previously associated with a steeper (higher) β slope [21]. It is thus possible that higher SWA in older mice indicate a steeper β slope which would bias narrowband estimates of rhythmic power in other frequencies, but this hypothesis still needs to be tested.

Recent experimental and modeling findings suggest that the β slope may reflect local neurophysiological parameters at the synaptic level, particularly those linked to the excitation-inhibition balance and networks dynamics [22, 23]. Beyond the characterization provided by the spectral slope, multifractal models also allow to capture the dynamics and variability of scale-free processes [24, 25]. Specifically, multifractal time series reflect a distribution of scaling exponents, indicating the coexistence of multiple scale-free processes operating at different timescales rather than a single, uniform scaling law as observed in monofractal systems [26, 27]. In neuroscience, increased multifractality has been reported locally in epileptogenic zones as well as in brain hubs engaging with multiple brain networks during cognitive tasks [28–30]. Examining multifractal properties during NREM sleep is therefore relevant for the hippocampus, a hub that is highly active during this state and importantly involved in overnight memory processing [31]. Notably, aging is associated with hippocampal hyperexcitability and lower specificity of hippocampal network interactions, phenomena that may manifest as local field potential (LFP) recordings with higher multifractality [32–34]. Characterizing how rhythmic and arrhythmic components from cortical and hippocampal activity evolve with age is thus relevant for understanding age-related changes in network dynamics during NREM sleep.

Here, we compared LFP power spectrum between younger and older mice in several cortical areas and within the hippocampus, while considering its rhythmic and arrhythmic components. We predicted age-related NREM sleep differences in both rhythmic and arrhythmic components specifically in anterior regions, whereas we expected age-related changes in multifractality parameters specifically for the hippocampus.

Methods

Experiments and animals

This experiment was performed in accordance with the guideline of the Canadian Council on Animal Care and approved by the Université Laval Committee on Ethics and Animal Research. Experiments were performed on 10 adult C57BL/6 J (7.6 months ±33.9 days, 4 females) and 11 older C57BL/6 J mice (15.7 months ±43.6 days; 6 females). Each mouse had a surgical implantation of LFP electrodes, after which they recovered for a week before starting recording.

Surgery and electrode implantation

The mice were first anesthetized with 1–2% isoflurane, the head was shaved and then fixed in a stereotaxic frame. The incision points were injected with a mixture of Bupivacaine (0.25%)/Lidocaine (0.5%). Ringer lactate (1 ml, i.p.) was injected for hydration. The mice head were cleaned with three passages of chlorhexidine gluconate (0.5%) in alternation with alcohol (70%) before the skin incision. After opening the skin above the skull, three alternating passages of a bleach solution (0.03% sodium hypochlorite) and hydrogen peroxide (3%) were used to clean the skull. Small holes (0.6 mm diameter) were drilled for the reference, anchoring screws, and LFP electrodes. We used custom-made electrodes stainless steel wires, 125 μm diameter, Perfluoroalkoxy (PFA)-insulated. Five electrodes were implanted in the cortex at a depth of 600 μm from the cortical surface, distributed along an antero-posterior axis 1.75 mm lateral to the midline on the left hemisphere. Approximate anteroposterior (AP) coordinates for targeted cortices are as follows: prefrontal cortex (+2.6 to 2.88 mm), primary motor cortex (M1, +1.0 mm), anterior somatosensory cortex (forelimb/trunk region: –0.5 mm), posterior somatosensory cortex (barrel field region, –1.75 mm) and visual cortex (V1: –3.5 mm). Another electrode was implanted in the contralateral ventral hippocampus CA1 (AP: –3.64, ML: 3.2, depth: 2 mm). This hippocampal region was selected due to its established involvement in sleep-dependent memory consolidation via a monosynaptic pathway with the prefrontal cortex [35, 36]. One stainless steel screw over the cerebellum was used as a reference. Two 75 μm diameter electrodes [single-stranded stainless-steel wire (PFA-insulated)], were inserted into the neck muscle to record the electromyographic (EMG) activity. All LFP electrodes, EMG electrodes, and the reference electrode were connected to an Omnetic connector and were covered and fixed with dental acrylic (Dentsply, Canada). Mice received subcutaneous injections of Ketoprofen (injectable Anafen, 5 mg/kg) and saline (0.5–1 ml) for 2 days post-surgery. Lab technicians daily evaluated mice until they were considered fit to undergo experimental protocol. A healthy condition (lack of bleeding, infection, or inflammatory symptoms around surgical site) and return of feeding behaviors were necessary for inclusion in the protocol.

Table 1. Number of available mice per recorded channel after artifact screening

Electrode	Younger (N = 10, 4 females)	Older (N = 11, 6 females)
Prefrontal	8 (4F)	11 (6F)
Motor	9 (6F)	10 (6F)
Somatosensory anterior	8 (6F)	10 (5F)
Somatosensory posterior	9 (3F)	9 (4F)
Visual	8 (4F)	9 (5F)
Hippocampus	10 (4F)	9 (5F)

Experimental conditions and electrophysiological recordings

After recovery, the mice were individually housed in a modified cage under a controlled 24-h light–dark cycle (lights off from 7 p.m. to 7 a.m.) and tethered to recording equipment for at least a week. Afterwards, individual cages were moved to a shielded room, where they were continuously recorded for another week. Mice had access to food and water *ad libitum*. Noise levels and entries were strictly controlled to ensure a quiet environment. In the shielded room, mice were connected to a ZIF-clip headstage, PZ2 preamplifier and RZ2 BioAmp Processor (Tucker-Davis Technologies, Florida, United States). The recordings were digitized at 3 KHz and bandpass filtered at 0.5–800 Hz for the LFP and at 10–300 Hz for the EMG.

Each animal original recordings were inspected offline using LabChart8 (ADInstruments, Colorado Springs, USA) to choose a period of 24 consecutive hours with minimal interruptions or recording issues. The selected 24 h of continuous recording per mouse was downsampled to 1 kHz and converted to Matlab format for further analysis. Signals from each electrode were also checked to ensure that recorded signals were adequate (not dominated by artifacts or persistent amplitude differences from other electrodes). Electrodes with persistent abnormal signal were excluded from all further analysis. The number of available mice per channel is shown in Table 1.

Table 2. NREM sleep epochs (expressed in minutes) included in the analyses

Period	Younger				Older			
	Mean	SD	Min	Max	Mean	SD	Min	Max
Light	358,21	19,25	315,60	385,67	403,18	51,97	335,47	527,20
Dark	207,70	47,21	139,73	259,80	246,19	64,94	126,60	370,33

Identification of vigilance states

We adapted a previously published semi-automated method [11] to generate a 24-h hypnograms for each mouse, with modifications for broader cortical electrode coverage. Power time courses were extracted in three frequency bands: cortical delta (0.5–4 Hz), hippocampal theta (5–9 Hz), and EMG activity (10–300 Hz). Power was computed using 4-s sliding windows (1-s step), resulting in power time courses at 1-s resolution. For each mouse, cortical delta power was averaged across all cortical electrodes (excluding hippocampus), theta from the hippocampal electrode (or visual cortex, if missing), and EMG averaged from both EMG leads.

Classification thresholds were manually defined for each mouse in 2-h intervals to account for time-of-day trends (i.e., progressive decrease of delta power across the light period), resulting in 6 intervals per light condition period. The following decision tree was applied on each 1-s timepoint:

1) High EMG → active wake
2) High cortical delta with low EMG → NREM sleep
3) High hippocampal theta with low EMG → REM sleep
4) Moderate EMG with low delta → quiet wake

Unclassified timepoints (e.g., high theta, high delta, and moderate EMG) were heterogeneous (mixed or transitional states) and were left as "undefined." Hypnograms were smoothed by reassigning isolated 1-s deviations to the surrounding state.

All 24-h hypnograms were visually reviewed by overlaying onto raw data (≥4 h per mouse, typically first 2 h of light and dark periods). Thresholds were adjusted if necessary to optimize state identification. State percentages were calculated separately for light and dark periods for statistical analyses.

For subsequent analyses targeted on rhythmic and arrhythmic components of NREM sleep, we identified all non-overlapping 4-s NREM sleep epochs and extracted raw signals from all electrodes. The total analyzed time per mouse is reported in Table 2.

Spectral analysis, rhythmic and arrhythmic components of NREM sleep LFP recordings

The "standard" power spectral density was computed from each 4-s epoch for all available channels [37]. For each 4-s epoch with the index '*i*', the power spectrum is designated by $p_i(f)$ (example from a younger mouse in Figure 1A). Standard power spectra were averaged separately during the light period (LP) and dark period (DP) for each electrode in each mouse, as described in the following equation:

$$P_I(f) = \frac{1}{n_I} \sum_{i \in I} p_i\ (f)$$

where I represents a period from the light–dark cycle i.e., a set of n_I epochs. Figure 1C illustrate the average power spectrum $P_I(f)$ from NREM sleep epochs averaged during the LP from recordings in a younger mouse. In the log–log scales, both spectra from single-epoch ($p_i(f)$) and their average ($P_I(f)$) do not favor any narrowband oscillatory mode but rather reveals a "scale-free" regime modeled with a power law of the form $1/f^{\beta_i}$. Up to a minus sign, the exponent $\beta_i$is the slope of the dashed line in Figure 1A. This slope, and consequently the scaling exponent, may change across different epochs, as shown in Figure 1B. Given this "dynamical" scale-free property across epochs, we used the following factorization of the power spectrum at each epoch, as in previous publications [18]:

$$p_i(f) = \frac{c_i}{f^{\beta_i}}\ e^{r_i(f)}$$

This multiplicative formulation highlights an exponential factor $e^{r_i(f)}$ that represent the rhythmic component present in the signal. To extract this factor, we first estimate the global offset c_i^* and the scaling exponent β_i^* using a linear regression of the power spectrum p_i in the log–log scales. Then, from the set of epochs in an interval I, we defined the so-called "rhythmic spectrum" $R_I(f)$ as the following average, which is depicted in Figure 1D.

$$R_I(f) = \frac{1}{n_I} \sum_{i \in I} \frac{f^{\beta_i^*}}{c_i^*}\ p_i\ (f)$$

The standard and rhythmic spectra (Figure 1C and D) were computed between 0.5 and 128 Hz. For the rhythmic spectrum, there was no scaling behavior at low frequency, and the scaling law was apparent starting at 4 Hz, therefore all rhythmic analyses on age-related differences are performed between 4 and 128 Hz.

Multifractal model of the arrhythmic component

The property that the scaling exponent is not unique and behaves with its own dynamics across vigilance states is well modeled with the multifractal formalism, which consider "local" scaling exponents to extract the multifractal spectrum (distribution of local exponents) [25, 38]. Wavelets leaders are increasingly used to describe multifractal scale-free activity as they can characterize the arrhythmic regime at a finer timescale [29, 39] which was previously applied to describe EEG recordings in rodents [25] and humans [30]. Here, we use the Wavelet Leader and Bootstrap based MultiFractal analysis (WLBMF) toolbox to estimate multifractal parameters in younger and older mice [40].

The multifractal distribution is estimated using the local and time-varying regularity parameters from the wavelet leaders (Hölder exponents). This distribution can be characterized by a set of log-cumulants in each epoch. Here we focus on the first two cumulants. The first-order cumulant (C1) represents the local regularity parameter most prevalent in the analyzed signal. C1 is closely related to the signal Hurst (H) exponent, quantifying its autocorrelation across time: $H = ½$ indicates the absence of correlation; $H > ½$ marks a persistent timeseries, with positive long-range correlation; $H < ½$ corresponds to an antipersistent timeseries, with negative long-range correlation. H is also in direct relationship with the spectral slope (β) derived from the power spectral density such as: $\beta = 2H\text{-}1$. Thus, persistent timeseries with $H > 0.5$ indicate a steeper spectral slope (increased

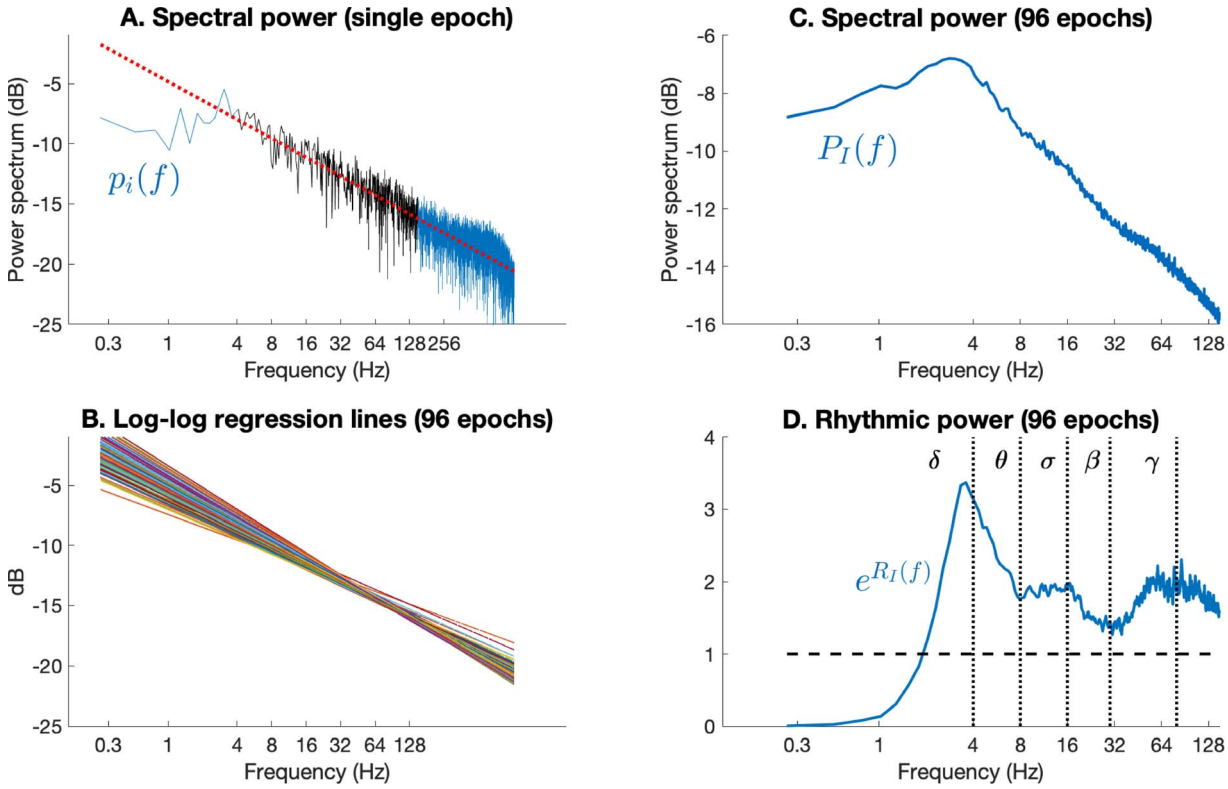

Figure 1. Epoch by epoch estimation of spectral and rhythmic power. (A) Power spectral density from one NREM sleep epoch taken from the first hour of the LP, in a single mouse from the motor cortex for illustrative purposes. The slope of the spectrum, depicted by the dashed straight line, is computed using the power between 4 Hz and 128 Hz (in black), where scaling behavior is evident. (B) Regression lines (4–128 Hz) estimated individually for each of the 96 NREM sleep epoch taken during the first two hours of a LP of a single younger mouse. (C) Average of the standard spectral power from the 96 NREM sleep LP epochs used in (B). (D) The rhythmic spectra (0.3–128 Hz) averaged from the 96 NREM sleep LP epochs used in (B). Compared to (C), the residual power in (D) is controlled for the influence of arrhythmic activity.

low-frequency activity and decreased high frequency activity). The second-order cumulant (C2) accounts for the width of the multispectral distribution, representing the dispersion (or variability) of exponents in each epoch. A very tight dispersion of exponents around C1 results in a C2 close to zero, indicating a monofractal signal. As the dispersion widens (i.e., higher multifractality), the C2 is more negative. Epochs that cannot be characterized by the model have a positive C2 and are excluded from our analysis.

From the multifractal spectrum of each 4-s epoch, we compute the first order-cumulant (C1), representing its most prevalent scaling exponent, which we name here H_m. Higher H_m indicate a steeper slope of the power spectrum, as expressed above. In each epoch, we also compute the absolute value of C2 as an indicator of the multifractal dispersion around H_m: higher Dispersion (D) indicate a more multifractal signal. For each mouse, H_m and D values are averaged from all epochs separately in the LP and DP.

Statistical analyses

Independent samples Student t-tests were used to analyze age group differences in percent of time in each state (%wake, %NREM sleep, %REM sleep, undefined states) for animals with at least three working electrodes (younger: n = 10; older: n = 11) in the LP and the DP.

We employed cluster-based nonparametric permutation tests to robustly test age group differences across frequencies in the standard Fourier and rhythmic residual spectra. Cluster-based permutation tests are particularly suitable to control familywise error rate (false-discovery, Type I errors) in electrophysiological data involving multiple frequency comparisons, and provide superior sensitivity compared to Bonferroni-based correction [41–43].

Age group contrasts in our cluster tests were conducted separately for the standard and rhythmic spectra at each electrode and LP/DP using custom Matlab (version 2022a) routines. For each test, a null hypothesis (no age-related differences between groups) was constructed using 5500 random permutations of individual spectral data into two arbitrary random groups. Each of the 5500 permutations involved the following steps:

1) Conducting independent samples t-tests at each frequency to identify differences (T-values) between random groups.
2) Forming clusters when frequency adjacent T-values reached a two-tail level threshold of $p<.05$. Smoothed clusters were obtained by grouping clusters with gaps <1 Hz.
3) For each cluster, we calculated the sum of T-values for all frequencies within. The largest cluster-level T-statistic (max-T) was retained from each permutation and included in the null hypothesis distribution. Each null hypothesis distribution included 5500 max-T values under the assumption of no random group difference.

The significance of each age contrast cluster was assessed from the maximal T-statistic in the null distribution, using a one-tailed threshold of $p\leq.05$. Only these primary clusters support statistical inference of age group difference. Because cluster tests are repeated in different electrodes and light condition, findings with $0.05 < p\leq.10$ are reported as exploratory trends when similar frequency bands are observed recurrently across conditions.

To evaluate the effects of age on H_m and D metrics from the multifractal model, linear mixed models (LMM) were computed using IBM SPSS 28.0.1. This method is better positioned than analyses of variances (ANOVAs) to account for missing values and heterogeneous variance between groups [44]. H_m and D were entered separately as dependent variables. Each variable was estimated using the Restricted Maximum Likelihood (REML) method. For each model, three fixed effects were parametrized: age (between subjects' factor, two levels), light period (repeated factor, two levels) and electrodes (repeated factor, six levels). All second-level interaction terms between age, electrode and light period were included in each model. An heterogenous autoregressive covariance structure (ARH1) was specified for the repeated factors to account for the covariance between electrodes. Convergence and significance of each model were required before interpreting results. Interaction and main effects are deemed significant at $p<.05$. When significant interactions were found, simple effect tests were conducted to test for age effect at each electrode and electrode effects in each age group. Subsequent pairwise contrasts were Bonferroni-adjusted.

Results

Sleep architecture in younger and older mice

We first evaluated whether the time spent in each vigilance states differed by age group (Figure 2). Younger (7.6 months ±33.9 days) and older (15.7 months ±43.6 days) mice showed no significant differences in the percentage of time spent in either state during the LP or DP: wake (LP: t-value = -0.35, p=.37; DP: t-value = 0.21, p=.42), NREM sleep (LP: t-value = -0.14, p=.44, DP: t-value = -0.53, p=.3), REM sleep (LP: t-value = -1.03, p=.16; DP: t-value = 0.39, p=.45) or transition states (LP: t-value = 0.90, p=.19; DP: t-value = 0.27, p=.39).

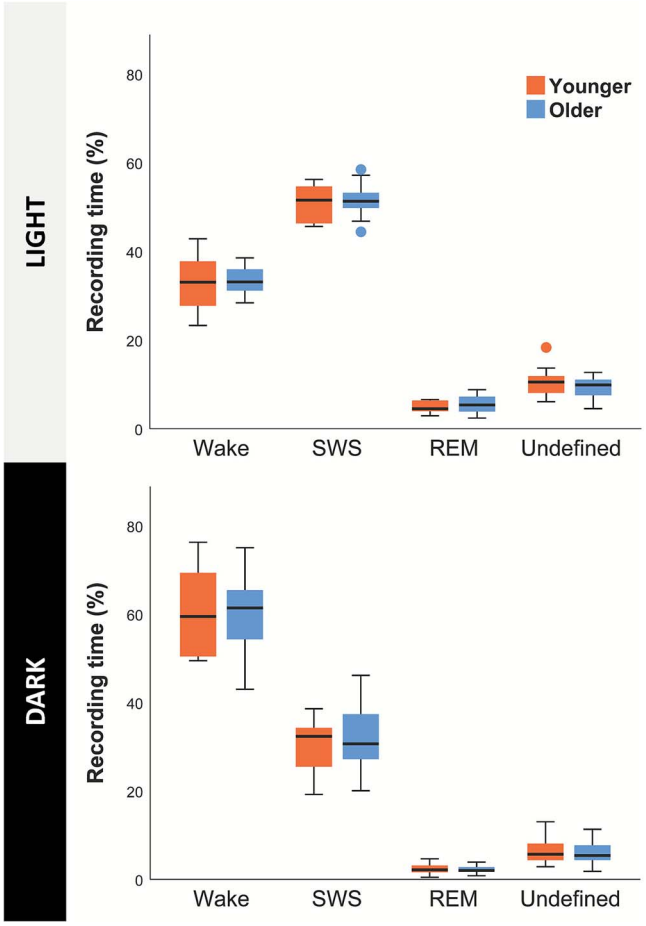

Figure 2. Percent of time spent in each vigilance state for younger and older mice. Boxplots for percent of total recording time in each vigilance state shown in LP (top) and DP (bottom) periods, separately for each state of vigilance. Younger mice are shown on the left of each state (orange), and older mice on the right (in blue). The boxes represent the interquartile range (IQR: The dispersion of values between the 1st and 3rd quartile), whereas the middle line represents the median. The whiskers extend to the minimum and maximum values that are not outliers (within 1.5 times the IQR from the first and third quartiles). Outliers, defined as values >1.5 times the IQR below the first quartile or above the third quartile, are shown as dots in the graph.

Older mice exhibit lower high-frequency and higher low-frequency spectral and rhythmic power in anterior electrodes

We sought to assess age differences in the standard and rhythmic power spectra during NREM sleep. *Visual inspection of the standard spectrum indicates that younger and older mice exhibit a linear 1/f decrease of amplitude according to frequency when plotted on a log–log scale, starting at around 4 Hz (Figure 3, top row). The rhythmic spectrum, shown in Figure 3 (third row), reveals residual spectral peaks, indicative of dominant and recurrent oscillations in the signal [15].*

We used permutation-based cluster tests for each electrode to evaluate the effects of age during the LP and DP on: (1) the NREM sleep standard spectral power and (2) the NREM sleep rhythmic power. Examination of NREM sleep spectral and rhythmic differences between younger and older mice highlighted age-related significant or trend-level differences only in the prefrontal and motor cortex. No significant or trends for age differences were found in spectral or rhythmic power for somatosensory cortices (anterior or posterior; see Supplementary Figure S1), nor in the visual cortex or in the hippocampus (Figure S2).

Significant age-related differences were found in the standard spectral power from the prefrontal cortex (Figure 3, top left panels). Old mice showed lower power across the theta-gamma range during both LP (10–86 Hz, cluster-corrected p=.04) and DP (10–77 Hz, cluster-corrected p=.04). In the motor cortex (Figure 3, top right panels), no significant differences were observed. Clusters indicating lower standard gamma power in older mice were observed at the trend level during both the LP (34–112 Hz, cluster-corrected p=.07) and the DP (36–117 Hz, cluster-corrected p=.08); however, these effects did not reach statistical significance.

A complementary pattern emerged for the rhythmic spectra in anterior electrodes, suggesting lower rhythmic gamma power in older mice. Older mice showed a significant age-related reduction in gamma power in the motor cortex during the LP (Figure 3, bottom right panels; 38–70 Hz, cluster-corrected p=.05). During the DP, a gamma cluster in a similar frequency range was also found in the motor cortex, but this effect did not reach statistical significance (41–75 Hz, cluster-corrected p=.06). In the prefrontal cortex (Figure 3, bottom left panels), no significant age-related differences were found in rhythmic power. A trend-level cluster indicating lower beta–gamma rhythmic power in older mice was found during the DP (33–60 Hz, cluster-corrected p=.06), whereas no corresponding effect was found during the LP (33–51 Hz, cluster-corrected p=.14). All other rhythmic clusters did not reach trend-level thresholds (p-values >0.10) and are thus not interpreted further.

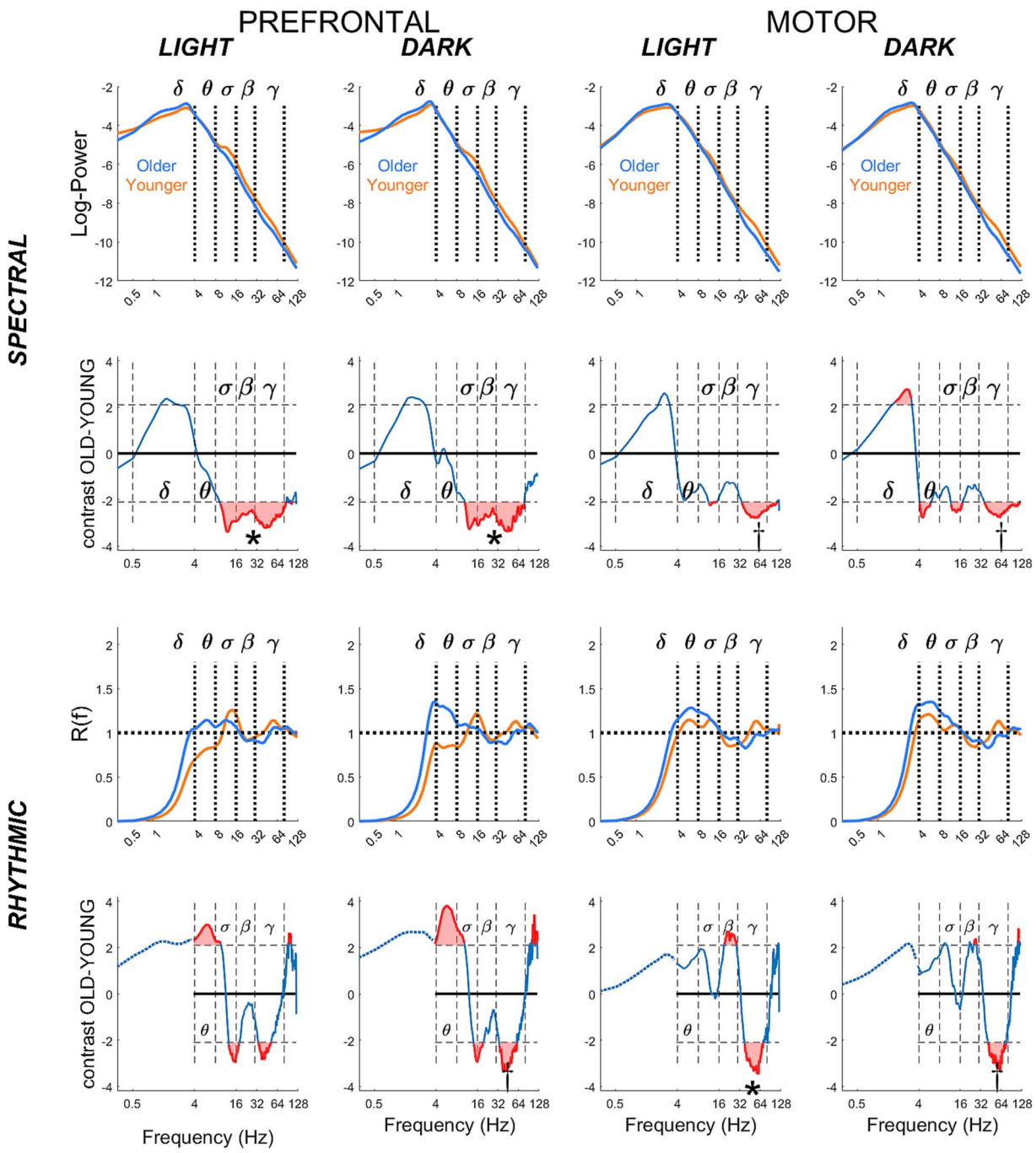

Figure 3. Spectral and rhythmic age-related differences in anterior cortical electrodes during NREM sleep. Analyses of age-related differences in standard spectral power (top two rows) and rhythmic power (bottom two rows) during NREM sleep, shown separately for prefrontal (left panels) and motor (right panels) electrodes across light and dark periods. With results from the cluster test analyses for age differences plotted below each spectrum. First and third rows: Standard spectral power (first row) and rhythmic power (third row) for younger (orange) and older (blue) mice. Second and fourth rows: T-values for age group contrasts at each frequency. Horizontal dashed lines indicate critical t-values = +/−1.96. Contiguous frequencies forming clusters are depicted in red. Significant clusters are marked with a star (*p<.05 in the permutation cluster-test) and trends with a cross (†, 0.05 ≤ p<.1 in the permutation cluster-test). For the rhythmic spectra, the cluster test starts at 4 Hz due to the absence of scale-free decay behavior at low frequencies (see methods).

Higher scaling exponents in the posterior somatosensory cortex of older mice

We investigated the arrhythmic component using a multifractal model. The H_m metric (C1) represents the most common scaling exponent in the signal, while the dispersion metric (D; C2) quantifies the variability of this scaling behavior (multifractality).

For H_m values, a significant age group by electrode interaction was found (F (5,57) =4.06, p=.002; Figure 4, top left panel). Although no significant age group differences emerged at individual electrodes, H_m values differed between electrodes specifically within the older group (F (5,93, p<.001), and not significantly in the younger group (F (5,98), p=.08). Within the older group, H_m values from the posterior somatosensory cortex were significantly higher

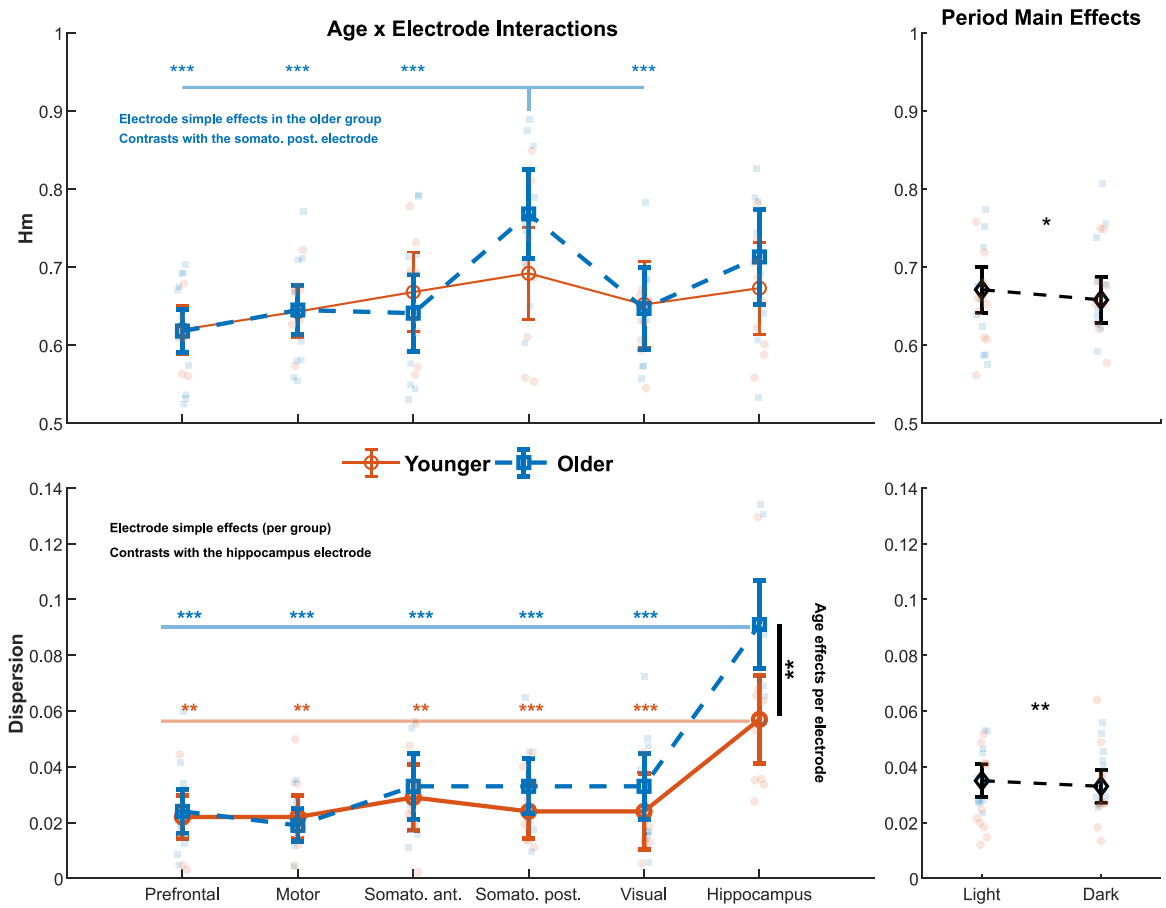

Figure 4. *Age- and period-related changes in the multifractal scaling exponent (H_m) and dispersion (D).* Linear mixed-effects models were fitted separately to the H_m (top row) and dispersion metric (bottom row) from the six intracranial electrodes (prefrontal, motor, anterior somatosensory, posterior somatosensory, visual, hippocampus) in younger (circles) and older (squares) mice. **Left panels** – Age × electrode interactions. Open circles (younger) and squares (older) show model-estimated marginal means ±95 % confidence intervals; mean connector bold lines represent electrode simple effects for each age group; translucent dots represent individual-mouse values averaged between light periods. For the H_m metric (top panel), the horizontal bar and stars at the top indicates the significance of the pairwise electrode contrasts within the older group only. In the dispersion panel (bottom panel), the bold vertical bar on the right show the significance of the age contrast for the hippocampal electrode. **Right panels** – Main effects of the light period. Model marginal means for the light and dark periods are displayed as diamonds ±95 % CI, connected by a dashed line. Each translucent point corresponds to one mouse (mean across electrodes within the period). Asterisks denote Bonferroni-corrected significance levels (***p<.001; **p<.01; *p<.05).

compared to all other cortical electrodes (all pairwise comparisons with the posterior somatosensory electrode: p<.001). No significant interactions were found between light/dark period and either electrode or age group. A main effect of light period was observed, with overall higher H_m values during the LP compared to the DP (F (1,126) = 11.16, p=.001; Figure 4, top right panel).

Higher dispersion of scaling exponents in the hippocampus of older mice

For the dispersion parameter D, a significant age group by electrode interaction was found (F (5,51 = 3.01, p=.019, Figure 4, bottom left panel). Older mice showed higher dispersion compared to younger mice at the hippocampal site only (F (1,25 = 9.46, p=.005). In both age groups, dispersion values at the hippocampus were significantly higher than those at all cortical regions (all pairwise comparisons: p<.05 in the younger group, p<.001 in the older group). Finally, a main effect of light period was observed, with overall higher dispersion during the LP compared to the DP (F (1,86) = 3.85, p=.05, Figure 4, bottom right panel).

Discussion

This study is the first to characterize age-related differences in rhythmic and arrhythmic components of the NREM power spectrum from cortical and hippocampal LFP recordings across the light–dark cycle in healthy mice. Because NREM sleep was the primary physiological state of interest in this study, all reported age-related effects should be interpreted within this vigilance state. Aging was associated with reduced rhythmic gamma activity specifically in anterior cortical regions, and with two distinct effects on scale-free dynamics during NREM sleep: higher dispersion in the hippocampus, and a regional peak over posterior somatosensory cortex. Together, these results indicate that aging impacts rhythmic and arrhythmic activity during NREM sleep in distinct brain areas.

We found an age-related reduction in gamma rhythmic power during NREM sleep specifically in the motor cortex during the LP. Trends for age-related reductions in gamma frequencies were observed during the DP in both motor and prefrontal cortices but did not reach significance. This convergent anterior profile suggest that aging is associated with reduced NREM sleep gamma rhythms in mice anterior cortex. Gamma rhythm occurs locally during the active state of slow waves and spindles [1, 45–48]. These rhythms are coordinated by basal forebrain PV interneurons [49], and can also be modulated by respiration [50]. Previous studies reported lower gamma rhythms during wake in the prefrontal cortex of older rodents [51, 52], along with impaired PV interneurons in the cortex and in the basal forebrain [53–55]. Because NREM

sleep gamma rhythms are thought to facilitate hippocampo-cortical communication underlying memory consolidation [56, 57], their age-related reduction could contribute to impairments in hippocampal-dependent memory consolidation with aging.

Using a multifractal framework, we found higher dispersion of scaling exponents in ventral CA1 compared to all other regions during NREM sleep. Furthermore, older mice showed higher dispersion than younger animals specifically in the hippocampus. Several studies have linked scaling exponents (or spectral slope) to the excitation-inhibition balance [22, 58–61], but the interpretation of multifractal metrics such as dispersion remains relatively new. The scaling exponent reflects the dominant 1/f scale-free regime (decay of power with frequency), whereas dispersion (D) quantifies the instability and variability of such scale-free regimes within a given analysis window [62]. Although previous studies associated multifractality with spectral "knees" (fixed transitions of the 1/f slope between distinct frequency ranges in each spectrum), dispersion remain conceptually distinct [63]. The dispersion metric captures the variability of scale-free activity across time: this dynamical aspect is not captured by frequency-domain metrics such as slope of knees. Such unstable scale-free dynamics have previously been associated with heightened neuronal excitability and irregular spiking activity at the cellular and population level [64–66]. In this context, higher dispersion in ventral CA1 is consistent with the intrinsically high excitability of neurons in this region [67–70]. The fact that older animals showed higher dispersion than younger animals specifically in the hippocampus aligns with age-related alterations of the excitation–inhibition balance [71], which predispose the aged hippocampus to hyperexcitability and reduced homeostatic control [72–74]. Together, these findings suggest that increased multifractal dispersion during NREM sleep may serve as a marker of excitability changes in the aging hippocampus. Future studies utilizing direct neuronal measures from identified neurons (e.g., calcium or voltage imaging) will be needed to confirm this association.

Older mice also showed a regional peak of their scaling exponent (H_m) in the posterior somatosensory cortex, resulting in a local maximal compared to other regions. Assuming a fractional Gaussian behavior ($\beta \approx 2H - 1$), higher H_m corresponds to a steeper aperiodic 1/f slope. In the hippocampal CA1 model, steeper slope has been linked to *stronger inhibition* [22]. This interpretation, however, may not straightforwardly apply to S1: aging studies in this region report reduced parvalbumin interneuron density, weaker perisomatic inhibition, and heightened pyramidal excitability [75–77]. Because the excitation–inhibition trajectory in mice is non-linear and begins to change ~4–6 months [71, 72], the regional peak we observed could reflect a transient increase in inhibitory tone. Yet, the relationship between scaling exponents and E/I balance is not consistent outside of the hippocampus [61], suggesting that alternative mechanisms should be considered. In the aged S1 cortex, pyramidal neurons show biophysical alterations acting as low-pass filters which could also lead to higher H_m values, including stronger I_h mediated sag current [77] and reduced distal dendritic spines [78]. *Thus, regional increases of H_m in older mice likely represent multifactorial alterations in microcircuit properties rather than a single process.*

Finally, we observed higher dispersion and H_m values during the light period compared to the dark period for all mice. Prior work similarly reported higher H_m during the LP in wake and REM sleep [25], and the 24 h variability of multifractal dispersion was recently shown to be altered in female Neuroligin-1 knockout mice during NREM sleep [79]. These findings indicate that arrhythmic metrics are sensitive not only to age or pathology, but also to circadian and homeostatic influences, consistent with evidence that neuronal activity regulating the E/I balance varies across these processes [80–82].

A few limitations of our study should be noted. First, both age groups were relatively mature (7 vs. 15 months old) and combined with our modest sample size (~10 mice per group), this may have limited statistical power and attenuated spectral and rhythmic findings previously reported (e.g., increased SWA and theta activity in aged rodents) [10, 11]. Second, while repeated effects were captured in our linear mixed models for multifractal measures, this was not feasible for the cluster-based permutation tests of rhythmic and spectral power. This may explain why age-related rhythmic reductions in the gamma-band appeared robust in the motor cortex for the LP, but only at trend level during the DP and in the prefrontal cortex. Age effects in NREM sleep rhythmic gamma remained consistent in direction and magnitude across LP and DP, suggesting these variations most likely reflect limited power. However, we cannot exclude that they also reflect modulation by circadian phase or homeostatic pressure. Finally, despite known sex differences in aging-related sleep patterns [83], our study lacked sufficient power to conduct sex-specific analyses (≈5 mice per sex per group).

By jointly considering rhythmic activity and scale-free dynamics, our study moves beyond the traditional rhythms-centric view of sleep electrophysiology. The coexistence of oscillatory and arrhythmic scale-free dynamics during NREM sleep suggests that memory consolidation emerges not only from synchronized rhythms but also from their interaction with scale-free fluctuations that shape local network dynamics [23,84]. Aging may thus alter sleep-dependent plasticity by altering the balance between these two forms of brain activity during NREM sleep. Whether similar joint changes extend to other vigilance states remains to be determined.

Supplementary material

Supplementary material is available at *SLEEP Advances* online.

Acknowledgments

We thank Sylvain Chauvette, Josée Seigneur, Anastasiia Ozuur, Sara Soltani, and Julia Potey for their invaluable help performing the surgeries and monitoring the experiments; special thanks to Sergiu Ftomov for electrode preparation and management, to Thomas Lehoux and Hamza Lahmimsi for data pretreatment, and Erika Bélanger-Nelson for mouse colony management and genotyping.

Author contributions

Jonathan Dubé (Conceptualization [equal], Data curation [equal], Formal analysis [lead], Investigation [lead], Methodology [equal], Visualization [equal], Writing—original draft [lead], Writing—review & editing [lead]), Justin Corbin (Formal analysis [supporting], Methodology [supporting]), Jimmy Hernandez (Conceptualization [supporting], Writing—review & editing [supporting]), Jean Marc Lina (Conceptualization [equal], Formal analysis [equal], Methodology [equal], Software [lead], Supervision [equal], Visualization [equal], Writing—review & editing [equal]), Valerie Mongrain (Conceptualization [equal], Funding acquisition [equal], Methodology [equal], Resources [equal], Supervision [supporting], Validation [equal], Writing—review & editing [equal]), Igor Timofeev (Conceptualization [equal], Funding acquisition [lead],

Investigation [equal], Methodology [equal], Project administration [equal], Resources [equal], Supervision [equal], Validation [equal], Writing—review & editing [equal]), and Julie Carrier (Conceptualization [equal], Funding acquisition [equal], Resources [equal], Supervision [lead], Validation [equal], Writing—review & editing [equal])

Funding

This research was supported by the following grants:

Fonds de recherche du Québec - Nature et technologie - Programme bilatéral de recherche collaborative Québec-Flandre #264146 and CRSNG/NSERC RGPIN-2016-05149 (J.C. and J.M.L).

Canada Research Chair in Sleep Molecular Physiology (V.M.)

CIHR grant PJT-183862 and NSERC grant RGPIN-2018-06291 (I.T.)

Disclosure statement

Financial disclosure: None.

Non-financial disclosure: None.

Data availability

The novel computer code and dataset used to create the Figure 2 are available onto this link: https://figshare.com/s/665edda282b9fc50cd3c.

All other data and codes will be shared on reasonable requests to the corresponding author.

References

1. Steriade M. Grouping of brain rhythms in corticothalamic systems. *Neuroscience*. 2006;**137**(4):1087–1106.
2. Girardeau G, Lopes-dos-Santos V. Brain neural patterns and the memory function of sleep. *Science*. 2021;**374**(6567):560–564.
3. Carrier J, Viens I, Poirier G, *et al*. Sleep slow wave changes during the middle years of life. *Eur J Neurosci*. 2011;**33**(4):758–766.
4. Martin N, Lafortune M, Godbout J, *et al*. Topography of age-related changes in sleep spindles. *Neurobiol Aging*. 2013;**34**(2):468–476.
5. Mander BA, Rao V, Lu B, *et al*. Impaired prefrontal sleep spindle regulation of hippocampal-dependent learning in older adults. *Cereb Cortex*. 2014;**24**(12):3301–3309.
6. Mander BA, Winer JR, Walker MP. Sleep and human aging. *Neuron*. 2017;**94**(1):19–36.
7. Jyoti A, Plano A, Riedel G, Platt B. EEG, activity, and sleep architecture in a transgenic AβPPswe/PSEN1A246E Alzheimer's disease mouse. *J Alzheimer's Dis*. 2010;**22**(3):873–887.
8. Jyoti A, Plano A, Riedel G, Platt B. Progressive age-related changes in sleep and EEG profiles in the PLB1Triple mouse model of Alzheimer's disease. *Neurobiol Aging*. 2015;**36**(10):2768–2784.
9. Panagiotou M, Vyazovskiy VV, Meijer JH, Deboer T. Differences in electroencephalographic non-rapid-eye movement sleep slow-wave characteristics between young and old mice. *Sci Rep*. 2017;**7**(1):43656.
10. Hasan S, Dauvilliers Y, Mongrain V, Franken P, Tafti M. Age-related changes in sleep in inbred mice are genotype dependent. *Neurobiol Aging*. 2012;**33**(1):195.e13–195.e26.
11. Soltani S, Chauvette S, Bukhtiyarova O, *et al*. *Front Syst Neurosci*. 2019;**13**:51.
12. McKillop LE, Fisher SP, Cui N, *et al*. Effects of aging on cortical neural dynamics and local sleep homeostasis in mice. *J Neurosci*. 2018;**38**(16):3911–3928.
13. Donoghue T, Haller M, Peterson EJ, *et al*. Parameterizing neural power spectra into periodic and aperiodic components. *Nat Neurosci*. 2020;**23**(12):1655–1665.
14. He BJ, Zempel JM, Snyder AZ, Raichle ME. The temporal structures and functional significance of scale-free brain activity. *Neuron*. 2010;**66**(3):353–369.
15. Buzsáki G, Draguhn A. Neuronal oscillations in cortical networks. *Science*. 2004;**304**(5679):1926–1929.
16. Muehlroth BE, Werkle-Bergner M. Understanding the interplay of sleep and aging: methodological challenges. *Psychophysiology*. 2020;**57**(3):e13523.
17. Ostlund B, Donoghue T, Anaya B, *et al*. Spectral parameterization for studying neurodevelopment: how and why. *Dev Cogn Neurosci*. 2022;**54**:101073.
18. Bódizs R, Szalárdy O, Horváth C, *et al*. A set of composite, non-redundant EEG measures of NREM sleep based on the power law scaling of the Fourier spectrum. *Sci Rep*. 2021;**11**(1):2041.
19. Finley AJ, Angus DJ, Reekum CM van, Davidson RJ, Schaefer SM. Periodic and aperiodic contributions to theta-beta ratios across adulthood. *Psychophysiology*. 2022;**59**(11):e14113, https://doi.org/10.1111/psyp.14113.
20. Voytek B, Kramer MA, Case J, *et al*. Age-related changes in 1/f neural electrophysiological noise. *J Neurosci*. 2015;**35**(38):13257–13265.
21. Horváth CG, Szalárdy O, Ujma PP, *et al*. Overnight dynamics in scale-free and oscillatory spectral parameters of NREM sleep EEG. *Sci Rep*. 2022;**12**(1):18409.
22. Gao R, Peterson EJ, Voytek B. Inferring synaptic excitation/inhibition balance from field potentials. *NeuroImage*. 2017;**158**:70–78.
23. Brake N, Duc F, Rokos A, *et al*. A neurophysiological basis for aperiodic EEG and the background spectral trend. *Nat Commun*. 2024;**15**(1):1514.
24. Abry P, Wendt H, Jaffard S, Didier G. Multivariate scale-free temporal dynamics: from spectral (Fourier) to fractal (wavelet) analysis. *Cr Phys*. 2019;**20**(5):489–501.
25. Lina JM, O'Callaghan EK, Mongrain V. Scale-free dynamics of the mouse wakefulness and sleep electroencephalogram quantified using wavelet-leaders. *Clocks Sleep*. 2019;**1**(1):50–64.
26. Lau ZJ, Pham T, Chen SHA, Makowski D. Brain entropy, fractal dimensions and predictability: a review of complexity measures for EEG in healthy and neuropsychiatric populations. *Eur J Neurosci*. 2022;**56**(7):5047–5069.
27. Dutta S, Ghosh D, Samanta S, Dey S. Multifractal parameters as an indication of different physiological and pathological states of the human brain. *Phys A: Stat Mech Appl*. 2014;**396**:155–163.
28. França LGS, Miranda JGV, Leite M, *et al*. Fractal and multifractal properties of electrographic recordings of human brain activity: toward its use as a signal feature for machine learning in clinical applications. *Front Physiol*. 2018;**9**:1767.
29. Rocca DL, Zilber N, Abry P, Wassenhove V van, Ciuciu P. Self-similarity and multifractality in human brain activity: a wavelet-based analysis of scale-free brain dynamics. *J Neurosci Methods* 2018;**309**:175-187, https://doi.org/10.1016/j.jneumeth.2018.09.010.
30. Gadhoumi K, Gotman J, Lina JM. Scale invariance properties of intracerebral EEG improve seizure prediction in mesial temporal lobe epilepsy. *PloS One*. 2015;**10**(4):e0121182.
31. Mišić B, Goñi J, Betzel RF, Sporns O, McIntosh AR. A network convergence zone in the hippocampus. *PLoS Comput Biology*. 2014;**10**(12):e1003982.

32. Leal SL, Yassa MA. Neurocognitive aging and the hippocampus across species. *Trends Neurosci*. 2015;**38**(12):800–812.
33. Huxter JR, Miranda JA, Dias R. The hippocampal physiology of approaching middle-age: early indicators of change. *Hippocampus*. 2012;**22**(9):1923–1940.
34. Bartsch T, Wulff P. The hippocampus in aging and disease: from plasticity to vulnerability. *Neuroscience*. 2015;**309**:1–16.
35. Binder S, Mölle M, Lippert M, *et al*. Monosynaptic hippocampal-prefrontal projections contribute to spatial memory consolidation in mice. *J Neurosci*. 2019;**39**(35):6978–6991.
36. Parent MA, Wang L, Su J, Netoff T, Yuan LL. Identification of the hippocampal input to medial prefrontal cortex in vitro. *Cereb Cortex*. 2010;**20**(2):393–403.
37. Welch P. The use of fast Fourier transform for the estimation of power spectra: a method based on time averaging over short, modified periodograms. *Ieee T Acoust Speech*. 1967;**15**(2):70–73.
38. Abry P, Wendt H, Jaffard S, Didier G. Multivariate scale-free temporal dynamics: from spectral (Fourier) to fractal (wavelet) analysis. *C R Phys*. 2019;**20**(5):489–501.
39. Wendt H, Roux SG, Jaffard S, Abry P. Wavelet leaders and bootstrap for multifractal analysis of images. *Signal Process*. 2009;**89**(6):1100–1114.
40. Wendt H, Abry P, Jaffard S. Bootstrap for empirical multifractal analysis. *IEEE Signal Process Mag*. 2007;**24**(4):38–48.
41. Maris E, Oostenveld R. Nonparametric statistical testing of EEG- and MEG-data. *J Neurosci Methods*. 2007;**164**(1):177–190.
42. Maris E. Statistical testing in electrophysiological studies. *Psychophysiology*. 2011;**49**(4):549–565.
43. Sassenhagen J, Draschkow D. Cluster-based permutation tests of MEG/EEG data do not establish significance of effect latency or location. *Psychophysiology*. 2019;**56**(6):e13335.
44. Yu Z, Guindani M, Grieco SF, Chen L, Holmes TC, Xu X. Beyond t test and ANOVA: applications of mixed-effects models for more rigorous statistical analysis in neuroscience research. *Neuron*. 2022;**110**(1):21–35.
45. Steriade M, Dossi RC, Paré D, Oakson G. Fast oscillations (20-40 Hz) in thalamocortical systems and their potentiation by mesopontine cholinergic nuclei in the cat. *Proc National Acad Sci*. 1991;**88**(10):4396–4400.
46. Valderrama M, Crépon B, Botella-Soler V, *et al*. Human gamma oscillations during slow wave sleep. *PloS One*. 2012;**7**(4):e33477.
47. Steriade M, Contreras D, Amzica F, Timofeev I. Synchronization of fast (30-40 Hz) spontaneous oscillations in intrathalamic and thalamocortical networks. *J Neurosci*. 1996;**16**(8):2788–2808.
48. Steriade M. The corticothalamic system in sleep. *Front Biosci*. 2003;**8**(4):d878–d899.
49. Kim T, Thankachan S, McKenna JT, *et al*. Cortically projecting basal forebrain parvalbumin neurons regulate cortical gamma band oscillations. *Proc Natl Acad Sci*. 2015;**112**(11):3535–3540.
50. Basha D, Chauvette S, Sheroziya M, Timofeev I. Respiration organizes gamma synchrony in the prefronto-thalamic network. *Sci Rep*. 2023;**13**(1):8529.
51. Insel N, Patron LA, Hoang LT, *et al*. Reduced gamma frequency in the medial frontal cortex of aged rats during behavior and rest: implications for age-related Behavioral slowing. *J Neurosci*. 2012;**32**(46):16331–16344.
52. Jessen SB, Mathiesen C, Lind BL, Lauritzen M. Interneuron deficit associates attenuated network synchronization to mismatch of energy supply and demand in aging mouse brains. *Cereb Cortex*. 2017;**27**(1):646–659.
53. Madhusudan A, Sidler C, Knuesel I. Accumulation of reelin-positive plaques is accompanied by a decline in basal forebrain projection neurons during normal aging. *Eur J Neurosci*. 2009;**30**(6):1064–1076.
54. Bañuelos C, Kittleson JR, LaNasa KH, *et al*. Cognitive aging and the primate basal forebrain revisited: disproportionate GABAergic vulnerability revealed. *J Neurosci*. 2023;**43**(49):8425–8441.
55. Ruden JB, Dugan LL, Konradi C. Parvalbumin interneuron vulnerability and brain disorders. *Neuropsychopharmacol*. 2021;**46**(2):279–287.
56. Zhang H, Fell J, Axmacher N. Electrophysiological mechanisms of human memory consolidation. *Nat Commun*. 2018;**9**(1):4103.
57. Ferraris M, Ghestem A, Vicente AF, *et al*. The nucleus Reuniens controls long-range Hippocampo–prefrontal gamma synchronization during slow oscillations. *J Neurosci*. 2018;**38**(12):3026–3038.
58. Semenova U, Popov V, Tomskiy A, Shaikh AG, Sedov A. Pallidal 1/f asymmetry in patients with cervical dystonia. *Eur J Neurosci*. 2021;**53**(7):2214–2219.
59. Gao R, Brink RL van den, Pfeffer T, Voytek B. Neuronal timescales are functionally dynamic and shaped by cortical microarchitecture. *eLife*. 2020;**9**:e61277. https://doi.org/10.7554/eLife.61277
60. Lombardi F, Herrmann HJ. Balance of excitation and inhibition determines 1/f power spectrum in neuronal networks. *Chaos: Interdiscip. J Nonlinear Sci*. 2017;**27**(4):047402.
61. Salvatore SV, Lambert PM, Benz A, *et al*. Periodic and aperiodic changes to cortical EEG in response to pharmacological manipulation. *J Neurophysiol*. 2024;**131**(3):529–540.
62. Wendt H, Jaffard S, Abry P. Multifractal analysis of self-similar processes. In: *2012, IEEE Statistical Signal Processing Workshop (SSP)*. Ann Arbor, MI, USA, 2012:69–72.
63. Lendner JD, Lin JJ, Larsson PG, Helfrich RF. Multiple intrinsic timescales govern distinct brain states in human sleep. *J Neurosci*. 2024;**44**(42):e0171242024.
64. Miller KJ, Honey CJ, Hermes D, Rao RP, denNijs M, Ojemann JG. Broadband changes in the cortical surface potential track activation of functionally diverse neuronal populations. *NeuroImage*. 2014;**85**:711–720.
65. Manning JR, Jacobs J, Fried I, Kahana MJ. Broadband shifts in local field potential power spectra are correlated with single-neuron spiking in humans. *J Neurosci*. 2009;**29**(43):13613–13620.
66. Rubfiaro AS, Godínez JR, Echeverría JC. Relationship in pacemaker neurons between the long-term correlations of membrane voltage fluctuations and the corresponding duration of the inter-spike interval. *J Membr Biol*. 2017;**250**(3):249–257.
67. McCormick DA, Contreras D. On the cellular and network bases of epileptic seizures. *Annu Rev Physiol*. 2001;**63**(1):815–846.
68. Johnson-Venkatesh EM, Khan MN, Murphy GG, Sutton MA, Umemori H. Excitability governs neural development in a hippocampal region-specific manner. *Development*. 2015;**142**(22):3879–3891.
69. Bhatia A, Moza S, Bhalla US. Precise excitation-inhibition balance controls gain and timing in the hippocampus. *eLife*. 2019;**8**:e43415.
70. Dougherty KA, Islam T, Johnston D. Intrinsic excitability of CA1 pyramidal neurones from the rat dorsal and ventral hippocampus. *J Physiol*. 2012;**590**(22):5707–5722.
71. Radulescu CI, Cerar V, Haslehurst P, Kopanitsa M, Barnes SJ. The aging mouse brain: cognition, connectivity and calcium. *Cell Calcium*. 2021;**94**:102358.

72. Radulescu CI, Doostdar N, Zabouri N, *et al*. Age-related dysregulation of homeostatic control in neuronal microcircuits. *Nat Neurosci*. 2023;**26**(12):2158–2170.
73. El-Hayek YH, Wu C, Ye H, Wang J, Carlen PL, Zhang L. Hippocampal excitability is increased in aged mice. *Exp Neurol*. 2013;**247**: 710–719.
74. Rozycka A, Liguz-Lecznar M. The space where aging acts: focus on the GABAergic synapse. *Aging Cell*. 2017;**16**(4):634–643.
75. Ueno H, Takao K, Suemitsu S, *et al*. Age-dependent and region-specific alteration of parvalbumin neurons and perineuronal nets in the mouse cerebral cortex. *Neurochem Int*. 2018;**112**: 59–70.
76. Calì C, Wawrzyniak M, Becker C, *et al*. The effects of aging on neuropil structure in mouse somatosensory cortex—a 3D electron microscopy analysis of layer 1. *PloS One*. 2018;**13**(7):e0198131.
77. Popescu IR, Le KQ, Ducote AL, Li JE, Leland AE, Mostany R. Increased intrinsic excitability and decreased synaptic inhibition in aged somatosensory cortex pyramidal neurons. *Neurobiol Aging*. 2021;**98**:88–98.
78. Ducote AL, Voglewede RL, Mostany R. Dendritic spines of layer 5 pyramidal neurons of the aging somatosensory cortex exhibit reduced volumetric Remodeling. *J Neurosci*. 2024;**44**(50):e1378242024.
79. Areal CC, Lemmetti N, Leduc T, *et al*. The absence of Neuroligin-1 shapes wake/sleep architecture, rhythmic and arrhythmic activities of the electrocorticogram in female mice. *Mol Brain*. 2025;**18**(1):38.
80. Brécier A, Borel M, Urbain N, Gentet LJ. Vigilance and Behavioral state-dependent modulation of cortical neuronal activity throughout the sleep/wake cycle. *J Neurosci*. 2022;**42**(24): 4852–4866.
81. Desrosiers J, Basha D. Cortical inhibition, plasticity, and sleep. *J Neurosci*. 2023;**43**(4):523–525.
82. Zong F, Min X, Zhang Y, *et al*. Circadian time- and sleep-dependent modulation of cortical parvalbumin-positive inhibitory neurons. *EMBO J*. 2023;**42**(3):e111304.
83. Deng Q, Li Y, Sun Z, *et al*. Sleep disturbance in rodent models and its sex-specific implications. *Neurosci Biobehav Rev*. 2024;**164**:105810.
84. Helfrich RF, Lendner JD, Knight RT. Aperiodic sleep networks promote memory consolidation. *Trends Cogn Sci*. 2021;**25**(8): 648–659.

SLEEP Advances, 2026, **7**, 1–12
https://doi.org/10.1093/sleepadvances/zpag012
Original Article